

Preparing Quantum Backflow States by Large Momentum Transfer

Yuchong Chen¹ and Yijun Tang¹

¹*Cavendish Laboratory, University of Cambridge,
JJ Thomson Avenue, Cambridge CB3 0US, United Kingdom*

A quantum backflow state refers to a quantum state exhibiting negative probability density flux albeit a completely positive momentum spectrum. Extending earlier work that uses single laser pulse to prepare quantum backflow state in an ultracold atomic BEC [1], we theoretical investigated flexible quantum backflow state preparation via large momentum transfer technique, which to our knowledge, has not been studied before. By combining atom interferometry theory and non-interacting BEC wave function, we solve for the evolution of a BEC wavepacket under atom interferometry sequence. Simulation results show a highly tunable backflow flux and critical density under our scheme, and can be manipulated to go beyond existing numbers.

I. Introduction

Quantum mechanics allows some states with purely positive momentum distribution to exhibit negative probability flux at some specific location and time; this phenomenon is known as quantum backflow. The effect was at first revealed in arrival time problem by Allcock [2], followed by detailed mathematically study by Brecken and Melloy [3], revealing a maximal amount of probability $c \approx 0.0384517$ that can flow backward over any time period for a free moving particle with positive momentum distribution in the nonrelativistic regime.

Over few decades, quantum backflow effect are further investigated, including new operator approach [4], on random wavefunction [5], during decay [6], ring geometry [7–9], higher dimension [10, 11], open quantum system [12–14], scattering in the presence of potential and defects [15, 16], many particle [17], effect of Boson/Fermion statistics [18] and in a periodic lattice [19].

Quantum backflow has not yet been observed in experiment. Potential experiments include a density measurement of an ultracold atomic BEC [1, 20], where a critical threshold exists that signifies quantum backflow. There is also attempt to loosen the constraint on purely positive momentum distribution, results in an "experimental-friendly" formulation [21, 22]. Although quantum backflow is still not observed, its classical analog is observed in optical setup recently [23–26].

A step towards observing quantum backflow is to prepare a state with large backflowing flux. In this paper we aim to extend existing approach with ultracold atomic BEC [1] by the means of atom interferometry[27]. We use highly tunable Large momentum transfer (LMT) pulses to split and recombine the atomic cloud, allowing control over momentum difference in the excited and ground component in the final backflow state. The paper is structured as follows: section II starts with reviewing state evolution under atom interferometry sequence followed by calculation of explicit expression of prepared backflow state. Section III displays sim-

ulation results, large backflow is seen under LMT sequence with a negligible classical backflow defect that is originated from residue negative momentum component instead of quantum backflow.

II. Theory

As shown in Fig.1, we start with a cloud of cold BEC of 2-level atom in a dipole trap followed by launching upward as in standard atom interferometry. Upon launching, a splitting pulse is applied to the cloud and separates it into two arms; the total state can be written as $|\Psi\rangle = c_f |\Psi_f\rangle + c_b |\Psi_b\rangle$. The $|\Psi_b\rangle$ arm has atoms in excited internal state and later exhibits LMT, gaining momentum via each laser pulse and propagates freely between pulses; the $|\Psi_f\rangle$ arm has atoms with ground internal state and undergoes free fall.

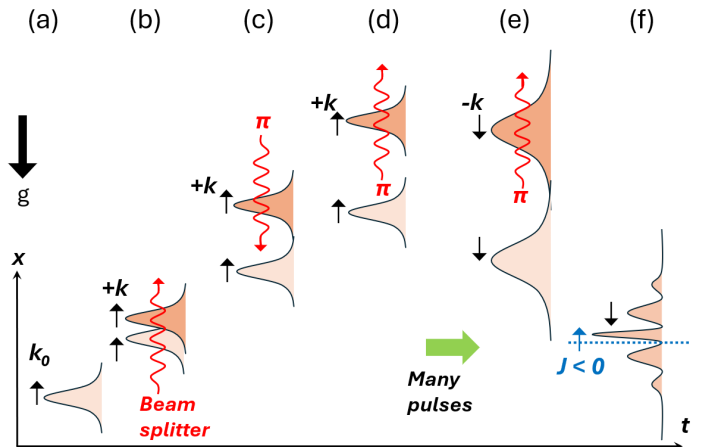


FIG. 1: Flexible quantum backflow state preparation procedure. (a) Initial cloud launching upward with momentum $\hbar k_0$ (b) Beam splitter pulse (not necessarily $\pi/2$). (c),(d),(e) π pulse on one arm to tailor momentum (f) Wavepackets encounter to form a backflow state.

The two arms encounter in the end and interfere, results in a quantum backflow state. By tuning pulse sequence after the splitting pulse, the negative probability flux and critical density can be tuned beyond literature value [1] with the cost of small cloud density modulation wavelength.

This framework consists of a calculation of state evolutions between laser pulses i.e. free evolutions under free fall, state modification during laser pulses and Backflow flux in the end of the sequence, we de-

scribe them in section A, B and C below.

A. Free propagation of BEC State

The free evolvement of a wavepacket between laser pulses can be described in a moving frame by a Galileo frame-transformation operator \hat{G} [27]

$$|\Psi\rangle = \hat{G}|\phi_{\text{CM}}(t)\rangle \otimes |A_i(t)\rangle = \exp\left(\frac{i}{\hbar}\int \mathcal{L}_c dt\right) \exp\left(-\frac{i}{\hbar}\hat{p} \cdot \vec{x}_c\right) \exp\left(\frac{i}{\hbar}\vec{p}_c \cdot \hat{x}\right) |\phi_{\text{CM}}(t)\rangle \otimes |A_i(t)\rangle \quad (1)$$

where the Lagrangian \mathcal{L}_c represents accumulation of action of COM (center-of-mass) motion, \vec{x}_c and \vec{p}_c are COM position and momentum, it follows that $\hat{p} \cdot \vec{x}_c$ is the spacial translation and $\vec{p}_c \cdot \hat{x}$ is the momentum boost due to transforming to a moving frame. The rest of Eq.1 is the tensor product between the BEC's center-of-mass state $|\phi_{\text{CM}}(t)\rangle$ and internal atomic state $|A_i(t)\rangle$. The spatial wavefunction of such a state is then

$$\langle \vec{x} | \Psi \rangle = e^{\frac{i}{\hbar} \int \mathcal{L}_c dt} e^{\frac{i}{\hbar} \vec{p}_c \cdot (\vec{x} - \vec{x}_c)} \langle \vec{x} - \vec{x}_c | \phi_{\text{CM}}(t) \rangle \otimes |A_i(t)\rangle \quad (2)$$

where $\langle \vec{x} - \vec{x}_c | \phi_{\text{CM}} \rangle$ is a wave function for the BEC state in the COM frame, we obtain this by first considering a non-interacting BEC wavefunction in the lab frame [1].

$$\begin{aligned} \psi(t) &= \frac{1}{\sqrt{b(t)}} \psi_0\left(\frac{x - v_1 t}{b(t)}\right) \\ &\times \exp\left[i \frac{m}{2\hbar} x^2 \frac{\dot{b}}{b} + ik_1 x \left(1 - \frac{\dot{b}}{b}\right) + i\beta(t)\right] \end{aligned} \quad (3)$$

where $\psi_0(x) = \frac{1}{\pi^{1/4} \sqrt{a_x}} \exp\left(-\frac{x^2}{2a_x^2}\right)$ is the initial wave function in a dipole traps given by the ground state of harmonic potential, $a_x = \sqrt{\hbar/(m\omega_x)}$ and ω_x is trap frequency. $\beta(t)$ is an irrelevant global phase, $\hbar k_1 = mv_1$ is the condensate velocity, and $b = \sqrt{1 + \omega_x^2 t^2}$ is the expansion rate. In the COM frame, all velocity terms are equal to 0. We then have the expression for the COM wave function

$$\langle x - x_c | \phi_{\text{CM}} \rangle = \frac{1}{\sqrt{b(t)}} \psi_0\left(\frac{x - x_c}{b(t)}\right) \exp\left[i \frac{m\dot{b}(x - x_c)^2}{2\hbar b}\right] \quad (4)$$

Physically this describes a BEC wavefunction localized at COM location x_c and expands in size by the rate $b(t)$, this form naturally contains negative momentum component and is the origin of classical backflow which is different from quantum backflow.

Experimentally, the atoms would be launched vertically. The action accumulated between two pulses separated by time Δt is therefore given by free fall motion:

$$\Delta S_C = \left(\frac{P_{\text{cn}}^2}{2m} - mgx_{\text{cn}}\right) \Delta t - P_{\text{cn}} g \Delta t^2 + \frac{1}{3} mg^2 \Delta t^3 \quad (5)$$

where P_{cn} and x_{cn} are the center-of-mass momentum and position of the atom after the n-th pulse, respectively. This completes the equation describing free evolution.

B. Pulse Influence

Now we calculate effect of laser pulse on our atomic cloud, the general scheme follows from [27]. Firstly, we can write the general state $|\Psi\rangle$ as a sum of two states, each having its own internal atomic energy, corresponding to the transition between ground and excited states

$$|\Psi_{\text{total}}\rangle = \int dp \sum_{i=1}^2 c_i(p) |p\rangle \quad (6)$$

Here we also decompose each state into momentum components for both ground and excited state with their momentum spectrum written $c_1(p)$ and $c_2(p)$. The general expression of transitions driven by a laser field in the short pulse time limit is given by:

$$\begin{pmatrix} c'_1(p) \\ c'_2(p + \hbar k) \end{pmatrix} = \begin{pmatrix} \Lambda_c & -i\Lambda_s e^{-i\phi_L} \\ -i\Lambda_s^* e^{i\phi_L} & \Lambda_c \end{pmatrix} \begin{pmatrix} c_1(p) \\ c_2(p + \hbar k) \end{pmatrix} \quad (7)$$

where $\Lambda_c = \cos(|\Omega|\tau/2)$, $\Lambda_s = \frac{\Omega}{|\Omega|} \sin(|\Omega|\tau/2)$, Ω is the Rabi oscillation frequency, k is laser momentum, ϕ_L is the laser phase, and τ is the duration of pulse. Tuning the pulse such that $|\Omega|\tau = \pi$ gives the expres-

sion for π pulse transition:

$$\begin{pmatrix} c'_1(p) \\ c'_2(p + \hbar k) \end{pmatrix} = \begin{pmatrix} 0 & -ie^{-i\phi_L} \\ -ie^{i\phi_L} & 0 \end{pmatrix} \begin{pmatrix} c_1(p) \\ c_2(p + \hbar k) \end{pmatrix} \quad (8)$$

In our simulation, the initial BEC wave packet from the dipole trap is first split into two arms containing different weights via a laser pulse that is not necessarily a $\pi/2$ pulse, the weighting in the two momentum arm will alter the backflow flux in the end. We will treat evolution of each arm individually, for example, apply a π pulse to an arm at ground state $|\Psi\rangle$ yields

$$\begin{aligned} |\Psi'\rangle &= \int dp c'_2(p) |p\rangle \\ &= -ie^{i\phi_L} \int dp c_1(p - \hbar k) |p\rangle \\ &= -ie^{i\phi_L} \int dp c_1(p) |p + \hbar k\rangle \\ &= -ie^{i\phi_L} \int dp c_1(p) e^{ik\hat{x}} |p\rangle \\ &= -ie^{i\phi_L} e^{ik\hat{x}} |\Psi\rangle \end{aligned} \quad (9)$$

The results is an absorption of photon of ground state to the excited with an increase of a recoil mo-

mentum aligned with laser direction. Generalizing to any internal state and pulse direction, we define an index μ which is 1 for ground state and -1 for excited state, and express the wave function immediately after the $n+1$ -th pulse by that after the n -th pulse:

$$\begin{aligned} \langle x|\Psi'\rangle &= -ie^{i\mu\phi_L} e^{\frac{i}{\hbar} \int \mathcal{L}_c dt} e^{i\mu k x_c} e^{\frac{i}{\hbar} (p + \mu \hbar k)(x - x_c)} \\ &\quad \times \langle x - x_c | \phi_{CM}(t) \rangle \otimes |A_i(t)\rangle \end{aligned} \quad (10)$$

Note that this expression differs from the state before pulse $\langle x|\Psi\rangle$ in Eq.2 by a laser ϕ_L , an extra momentum boost $(p + \mu \hbar k)$, as well as a global phase shift $\mu k x_c$.

C. Probability Flux and Critical Density

We can now trace the evolution of each arm separately. In simulation, one arm undergoes completely free full and is not subject to any laser influence. This is the free arm and its final form at encounter time T_f can be directly solved by Eq.2, Eq.4, and Eq.5. We denote the state of the free evolving arm as $|\Psi_f\rangle$, its spatial wavefunction is then

$$\begin{aligned} \langle x|\Psi_f\rangle &= \frac{1}{(1 + \omega_x^2 T_f^2)^{1/4} \pi^{1/4} \sqrt{a_x}} \exp \left[\frac{i}{\hbar} \left(\frac{1}{2} m v_0^2 T_f - m v_0 g T_f^2 + \frac{1}{3} m g^2 T_f^3 \right) \right] \exp \left[\frac{i}{\hbar} m (v_0 - g T_f) (x - x_c) \right] \\ &\quad \times \exp \left[-\frac{(x - x_c)^2}{2 a_x^2 (1 + \omega_x^2 T_f^2)} \right] \exp \left[i \frac{m}{2 \hbar} (x - x_c)^2 \frac{\omega_x^2 T_f}{1 + \omega_x^2 T_f^2} \right] \otimes \exp \left(-\frac{i}{\hbar} E_\lambda T_f \right) |\lambda\rangle \end{aligned} \quad (11)$$

where E_λ is the energy of free-arm's internal state.

The momentum-transferred arm exhibits change in momentum at each pulse instant. Hence, we first express the state immediately after the $n+1$ -th pulse by

$$\begin{aligned} \langle x|\Psi_{n+1}\rangle &= -i \exp(i\mu_n \phi_L) \exp(i\mu_n k_{n+1} x_{n+1}) \exp \left[\frac{i}{\hbar} \left(\frac{1}{2} m v_{c,n}^2 \Delta t - m g x_{c,n} \Delta t - m v_{c,n} g \Delta t^2 + \frac{1}{3} m g^2 \Delta t^3 \right) \right] \\ &\quad \times \exp \left[\frac{i}{\hbar} m v_{c,n+1} (x - x_c) \right] \frac{1}{(1 + \omega_x^2 t_{n+1}^2)^{1/4} \pi^{1/4} \sqrt{a_x}} \exp \left[-\frac{(x - x_c)^2}{2 a_x^2 (1 + \omega_x^2 t_{n+1}^2)} \right] \\ &\quad \times \exp \left[i \frac{m}{2 \hbar} (x - x_c)^2 \frac{\omega_x^2 t_{n+1}}{1 + \omega_x^2 t_{n+1}^2} \right] \tilde{\phi}_{L,tot} \tilde{\psi}_{i,tot} \tilde{\Psi}_S \otimes \exp \left(-\frac{i}{\hbar} E_{\mu_n} \Delta t \right) |\mu_{n+1}\rangle \end{aligned} \quad (12)$$

where the subscript n represents the physics quantity evaluated at a time point immediately after the n -th pulse. The first two terms are laser phase and the $n+1$ -th pulse influence; the first exponential

parameters of the n -th pulse, we denote it as $|\Psi_{n+1}\rangle$. Assuming that pulse duration $\tau \ll \Delta t$ to ignore influences other than laser pulse we get the spatial wavefunction

factor is the action between two pulses, followed by translation to the COM frame, and the COM wave function Eq.4 evaluated at t_{n+1} . $\tilde{\phi}_{L,tot}$, $\tilde{\psi}_{i,tot}$, and $\tilde{\Psi}_S$ stand for the laser phase, internal evolution,

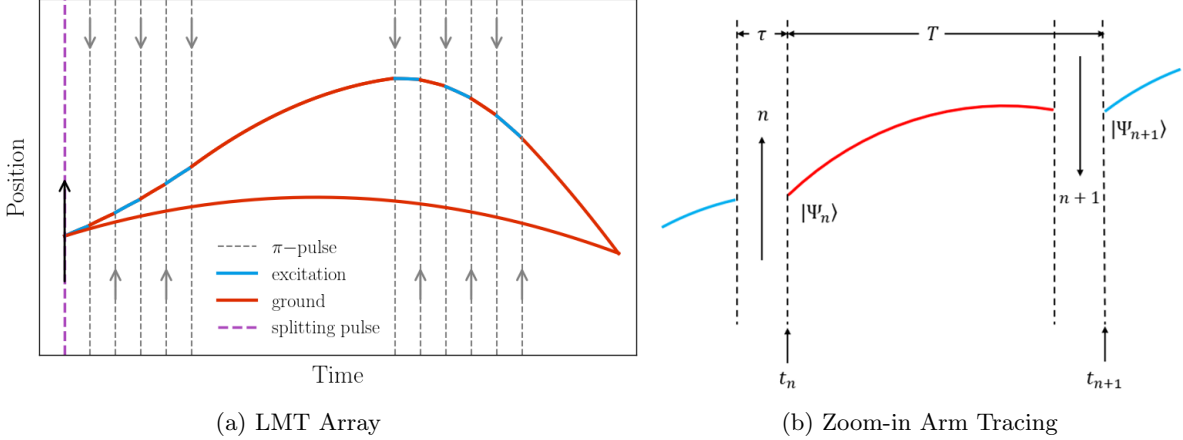


FIG. 2: Qualitative illustration of LMT setup. (a): overall setup of LMT array. The left most arrow represents splitting pulse. The subsequent π -laser pulses only address on one arm, causing it to alternate between ground and excitation state as well as transferring momentum boost. (b): Zoom in view of two consecutive pulses. Duration of each pulse is fixed as τ , while pulse interval $T = t_{n+1} - t_n$ may vary. States labeled as $|\Psi_n\rangle$ and $|\Psi_{n+1}\rangle$ are defined as the quantum state right after each pulse.

and action phases accumulated through all previous motion. $|\mu_n\rangle$ represents the initial internal state after the n -th pulse, thus time evolution is explicitly written as $\exp(-iE_{\mu_n}\Delta t/\hbar)$.

To convenience later calculation, we group Eq.11 and Eq.12 into evolution phases and position-dependent terms. We further note that the two arms do not encounter each other right after the last pulse. Allowing a traveling time of ΔT_f after T_N which is the time of the final pulse. Each arm's wave function at encounter can be written as:

$$\begin{aligned} \langle x|\Psi_f\rangle &= \langle x - x_c|\phi_{\text{CM}}(T_f)\rangle \exp[i\theta_f(E_\lambda, v_0, T_f)] \\ &\times \exp\left[\frac{i}{\hbar}m(v_0 - gT_f)(x - x_c)\right] \end{aligned} \quad (13)$$

$$\begin{aligned} \langle x|\Psi_b\rangle &= \langle x - x_c|\phi_{\text{CM}}(T_f)\rangle \exp[i\theta_b(\{E_{\mu_n}\}, \{t_n\}, \{k_n\})] \\ &\times \exp\left[\frac{i}{\hbar}m(v_N - g\Delta T_f)(x - x_c)\right] \end{aligned} \quad (14)$$

where $T_f = T_N + \Delta T_f$ is the time of encountering. As such, we have obtained the final wave function for the two arms in terms of the common COM state. We can then write the total wave function as a weighted sum of the two arms

$$\begin{aligned} \langle x|\Psi\rangle &= \langle x|\Psi_f\rangle \\ &\times [c_f + c_b \exp\left(\frac{i}{\hbar}m(v_N - gT_f)(x - x_c)\right) \\ &\times e^{(i\theta_b - i\theta_f)}] \end{aligned} \quad (15)$$

where c_f and c_b are weights tunable by adjusting the initial pulse duration. Based on Eq.11, $\langle x|\Psi_f\rangle$ can

also be decomposed to a real component and a phase factor $\langle x|\Psi_f\rangle = R(x, t)e^{i\theta(x, t)}$. The critical probability density below which quantum backflow would occur is given by [1]:

$$\rho_{\text{crit}} = \frac{q}{q + 2\nabla\theta(x, t)} |R(x, t)|^2 (|c_f|^2 - |c_b|^2) \quad (16)$$

where

$$q = \frac{m}{\hbar}(v_N + gT_f - v_0) \quad (17)$$

$$\begin{aligned} R(x, t) &= \frac{1}{(1 + \omega_x^2 T_f^2)^{1/4}} \frac{1}{\pi^{1/4} \sqrt{a_x}} \\ &\times \exp\left[-\frac{(x - x_c)^2}{2a_x^2} \frac{1}{1 + \omega_x^2 T_f^2}\right] \end{aligned} \quad (18)$$

$$\begin{aligned} \theta(x, t) &= \frac{1}{\hbar} \left(\frac{1}{2}mv_0^2 T_f - mv_0 g T_f^2 + \frac{1}{3}mg^2 T_f^3 - E_\lambda T_f \right) \\ &+ \frac{1}{\hbar} \left[m(v_0 - gT_f)(x - x_c) + \frac{m}{2} \frac{\omega_x^2 T_f}{1 + \omega_x^2 T_f^2} (x - x_c)^2 \right] \end{aligned} \quad (19)$$

while the probability flux is given by [1]; here we have extended the calculation to account for c_f, c_b being complex:

$$\begin{aligned} \frac{m}{\hbar} J(x, t) &= \nabla\theta |\Psi|^2 + q |R|^2 |c_b|^2 \\ &+ q |R|^2 \text{Re}(c_f^* c_b e^{iqx + i\theta_b - i\theta_f}) \end{aligned} \quad (20)$$

III. Simulation Result

A. Setup

In simulation, we consider a hypothetical case of a non-interacting ^{88}Sr BEC and its $^1S_0 - ^3P_1$ transition for LMT, with laser wavelength of 689 nm. The 3P_1 excited state has a life time of $21.6 \mu\text{s}$ which makes it suitable for LMT. Up to date, a $141\hbar k$ LMT had been achieved in ^{88}Sr atom interferometer. [28].

We start with a BEC cloud launching upward at initial velocity $v_0 = 0.2 \text{ ms}^{-1}$ with a spatial profile of a dipole trap of trap frequency $\omega_x = 2\pi \times 70 \text{ s}^{-1}$ [29]. A beam splitter pulse of tunable duration τ then splits the atoms into two arms with coefficient c_b, c_f according to Eq.7. Fig.3 shows the set up used for later evolution. Only one arm will be addressed by laser due to narrow linewidth of the transition and doppler shift, we will call the un-addressed arm by free arm and the other by pulsed arm. The free arm will undergo free fall without influence from the lasers before encountering the pulsed arm. The pulsed arm is initially at excited state due to beam splitting pulse; it later undergoes 1 LMT pulses of wavelength 689nm and duration of a π pulse, thus transforming all population to the ground state. The pulsed arm then travels upward for 4ms before being deflected downward by two pulse arrays separated by 4ms as well. All adjacent pulses are separated by $11 \mu\text{s}$. The sequence is optimized to give the free arm a lowest downfall velocity possible at encountering to maximize momentum difference between the two arms.

B. Classical Backflow

We must first confirm that there exists negligible negative momentum component which give rises to classical backflow, where the increase in probability at negative regions are not due to quantum backflow which is an interference effect but rather the expansion of Gaussian wavepacket as it propagates. Experimentally, this is achieved by setting $mv/\hbar \gg 1/a_x$ and $R_0 < v/\omega_x$, where R_0 is the initial width of the wavepacket [1]. To quantify whether such effect is present, we transform $\langle x|\Psi\rangle$ to momentum basis, as shown in Fig.4, and verify that there is indeed negligible negative component. The two peaks correspond to the velocities of the two arms.

C. Probability Flux

The total wave function at encountering point is calculated to find the probability flux at its vicinity. Fig.5a shows an example backflow flux distribution

in space for $\Omega\tau = 0.6\pi$ as initial splitting pulse. Near COM, approximately 1/6 of J is negative. Fig.5b outlines the area where evident backflow occurs. Another dominant feature of flux distribution is the fast oscillatory pattern. This occurs since in Eq.20 J includes a sinusoidal term with oscillating frequency q , which is related to momentum difference of the two arm. For our case, the velocity difference at encounter is 0.079ms^{-1} .

In Fig.6a we show the density for $|\Psi\rangle$ near COM in blue, as well as the critical density in orange, below which quantum backflow may occur. Both density curves are normalized by the maximum of $|\Psi|^2$. The final state's density has a Gaussian profile with oscillatory pattern. The Gaussian shape arises from the ground state of dipole trap, whereas the sinusoidal oscillation originates from the position-dependent exponential in Eq.15. From Fig.6b, the maximum of ρ_{crit} is 15.21%, and near x_c minimum of $|\Psi|^2$ is 0.04%.

D. Parameter Tuning

We now show that the amount of backflow can be accurately controlled by changing the beam splitter pulse's duration τ . By Eq.7, this is equivalent to altering the Rabi oscillation phase $\Omega\tau$ which the initial arm from dipole trap undergoes. It thus tunes the two split arms' component c_b and c_f .

Assuming that the Rabi frequency is a real number, we take a sweep through the possible Rabi oscillation phases $\Omega\tau \in [0, 4\pi]$ with $c_1(p) = 1, c_2(p) = 0$ as input to Eq.7, which is equivalent to a condensate in ground state entering the splitting pulse. The $\Omega\tau$ values generate a grid of $c_b = \cos(\Omega\tau/2), c_f = -i \sin(\Omega\tau/2)$. For each set of coefficients, the flux is then calculated with velocities and LMT settings used in section III A.

We define backflow rate as the area of J below zero, colored red in Fig.5b. This rate is an integration of space, characterizing the size of region where backflow may occur for observation. Fig.7a plots backflow rate against $\Omega\tau$. The graph is symmetric about $\Omega\tau = \pi$; each side exhibits one backflow peaks. There are also regions where no backflow occur at all, at $\Omega\tau \in [0, \pi/2] \cup [3\pi/2, 2\pi]$. They correspond to phases that give $|c_f|^2 < |c_b|^2$. From Eq.16, this leads to negative ρ_{crit} and backflow is impossible to occur. The zero well at $\Omega\tau = \pi$ corresponds to a π -pulse, which would turn the initial ground state arm to a purely excited state arm and zero backflow is expected.

We fix on x where the maximum backflow occurs,

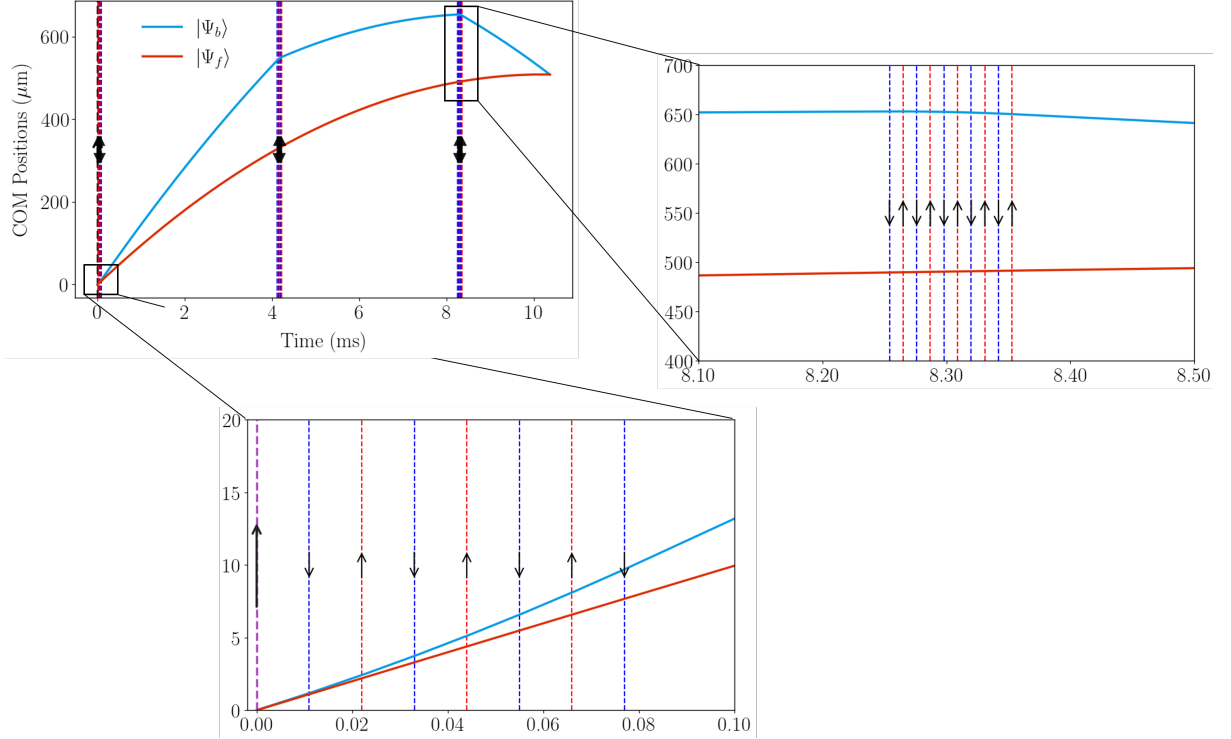


FIG. 3: Simulation setup for preparing backflow states. Pulses only address $|\Psi_b\rangle$ (blue curve), hence it undergoes large momentum transfer while $|\Psi_f\rangle$ (red curve) evolves freely. At $t = 0$, a splitting pulse (shown as purple dashed line) stimulates a proportion of the condensate into excited state and creates initial velocity difference. $|\Psi_b\rangle$ is then accelerated by consecutive π -pulses.

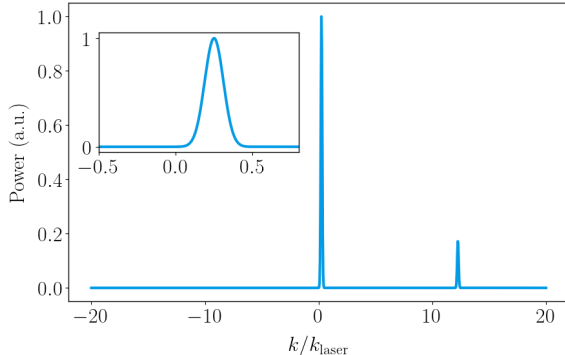


FIG. 4: Momentum spectrum of final combined state $\langle k|\Psi\rangle$. The two peaks correspond to the two arms' momentum at encounter. No negative momentum is observed.

we plot J for the $\Omega\tau = 0.75\pi$ peak in Fig.8. The maximum negative flux is now below -500 s^{-1} and approximately 1/3 of J is negative. Comparing Fig.6a and Fig.9, we note that the $\Omega\tau = 0.75\pi$ setting sustains similar $\rho < \rho_{\text{crit}}$ region ($\sim \pm 20 \mu\text{m}$), since the size of condensate is mainly determined by the oscillation strength a_x and propagation time, which are constant across simulations. For the probability density, the minimum $|\Psi|^2$ near x_c is

now 18.39%, and the maximum ρ_{crit} is 39.79% which is more than twice the value obtained in earlier proposal[1] that reads $\rho_{\text{crit}} \approx 17\%$.

It is also instructive to investigate how real weight coefficients influence backflow. We directly change c_b and c_f while keeping $c_b^2 + c_f^2 = 1$. As shown in Fig.7b, real coefficients yield only one peak, and no backflow is present at the two ends since the limiting cases of single wavepacket, which no interference occurs thus no backflow. The maximum backflow rate is similar to that of complex weights. The threshold also skews to the right with backflow no longer occurring for $c_b > 1/\sqrt{2}$, where $c_f < c_b$ and ρ_{crit} is negative. The maximum backflow rate occurs at $c_b = 0.37$. Comparing Fig.7a and Fig.7b, real coefficients lead to wider window for backflow to occur. To achieve $c_f, c_b \in \mathcal{R}$ we will need additional pulses after splitting pulse, and will introduce additional phase shift before LMT begins.

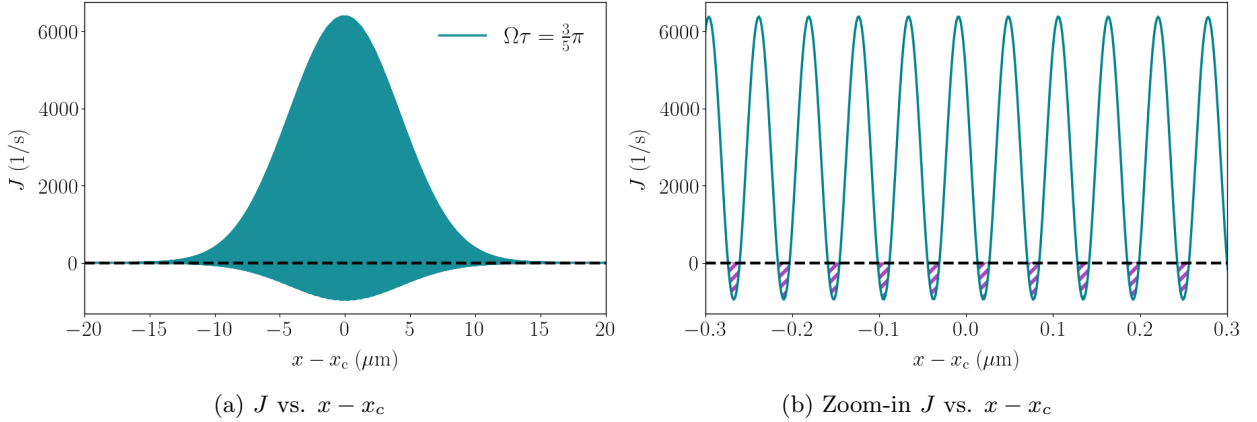


FIG. 5: Example probability flux J for initial splitting parameter $\Omega\tau = 0.6\pi$ plotted against relative position to COM $x - x_c$. (a) Overall view; a considerable proportion of flux is below zero, demonstrating successful backflow. (b) Zoom-in view of positions $0.3 \mu\text{m}$ near COM; dashed regions correspond to backflow occurring.

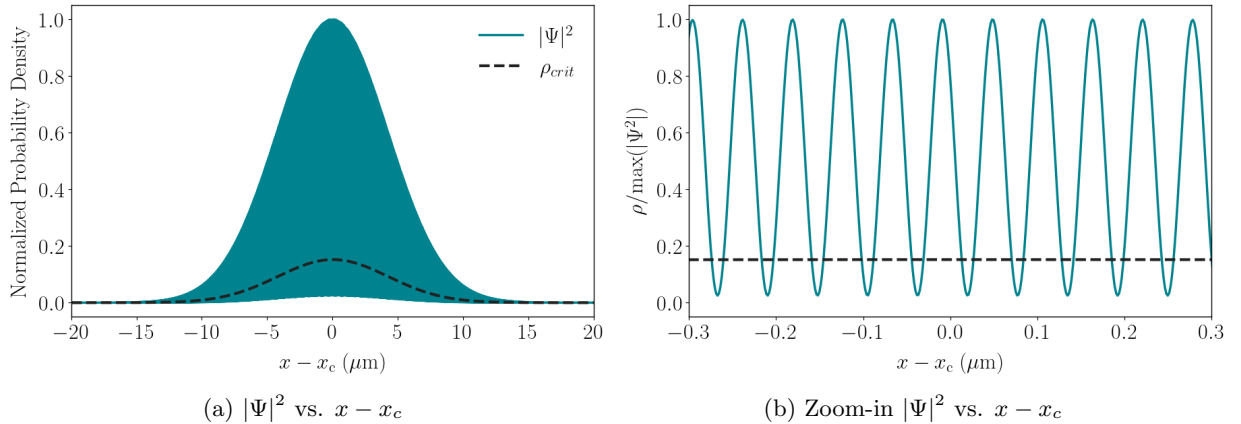


FIG. 6: Probability density distribution for the simulation in Fig.5. (a) overall density follows Gaussian profile with oscillatory pattern; black dashed line represents ρ_{crit} . A narrow spatial range near x_c is observed to have $|\Psi|^2$ evidently smaller than ρ_{crit} . (b) Zoom-in view near x_c , ρ_{crit} . Values are normalized by $|\Psi|^2$'s maximum value. ρ_{crit} has maximum of 15.21%, while local minimum of $|\Psi|^2$ is 0.04%.

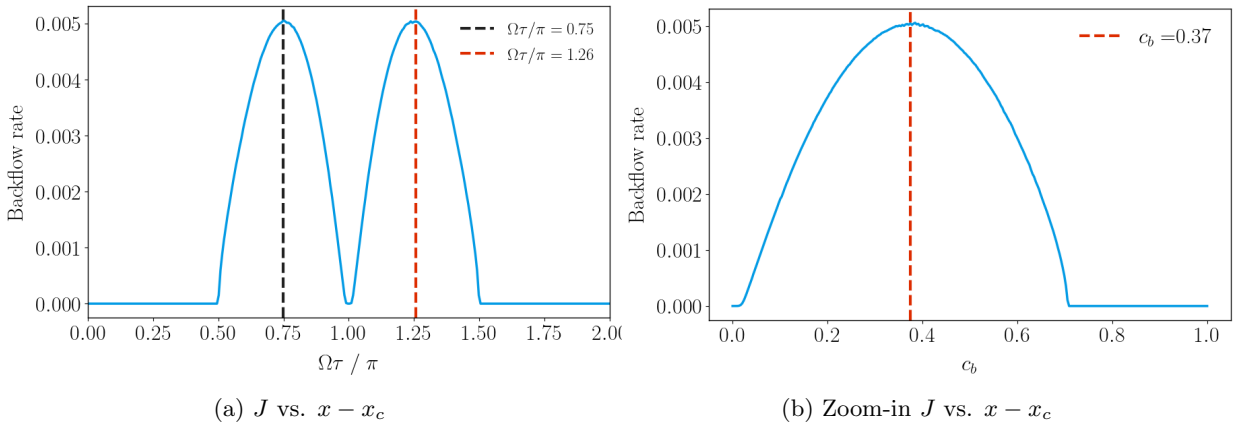


FIG. 7: (a) Backflow rate plotted against Rabi oscillation phase in complex regime. The complex coefficients opens up different windows of quantum backflow. (b) Backflow rate plotted against c_b . One single peak is present with similar backflow rate to complex weight coefficient. For $c_b > 1/\sqrt{2}$, ρ_{crit} is negative and hence no backflow occurs.

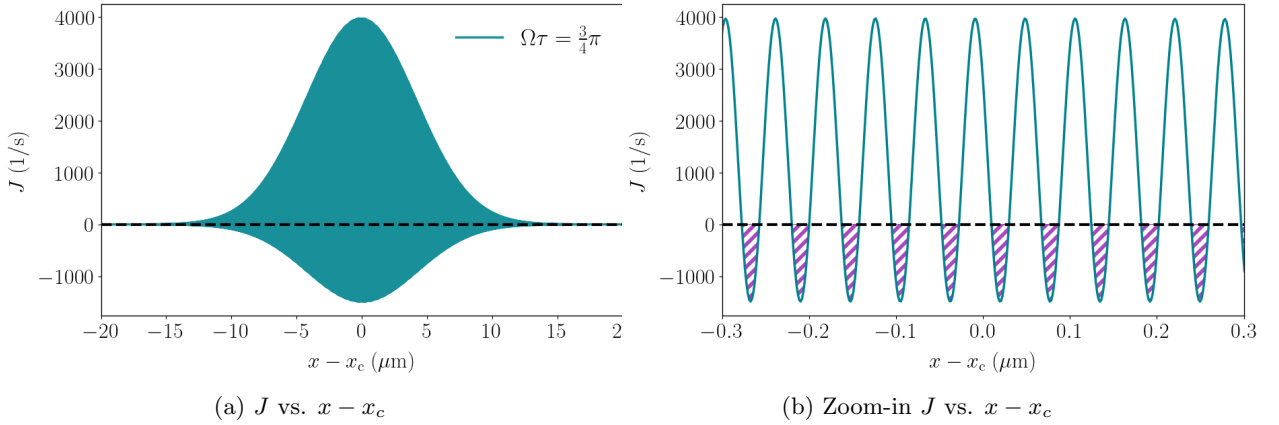


FIG. 8: Maximum probability flux J plotted against $x - x_c$. Parameter used $\Omega\tau = 0.75\pi$. (a) Overall view. (b) Zoom-in view; The dashed regions have about twice the area seen in Fig.5b.

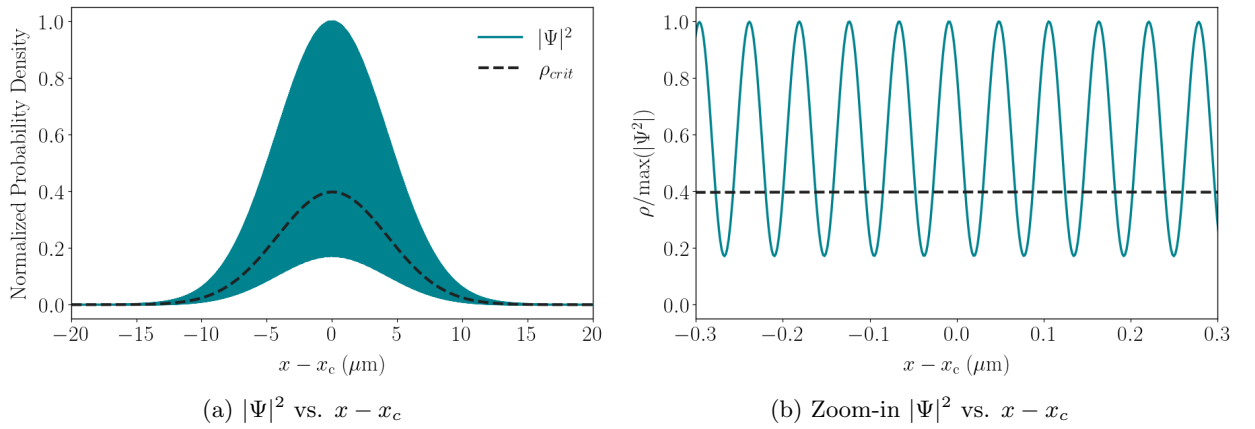


FIG. 9: Probability density distribution at maximum backflow, normalized by maximum of $|\Psi|^2$. (a) Regions with $|\Psi|^2 < \rho_{\text{crit}}$ span through spaces near COM. (b) Zoom-in view. Maximum of ρ_{crit} is 39.79%, whereas relative minimum of $|\Psi|^2$ around x_c is 18.39%.

IV. Conclusion

We have proposed a method based on LMT atom interferometry to flexibly prepare large backflow state, the tunability lies in the introduction of a whole brand new parameter space of LMT sequence, including initial beam splitting pulse and consecutive π -pulses. We presented simulation examples with realistic experimental parameters, results show highly tunable final quantum backflow state with negligible classical backflow, i.e. negative mo-

mentum component. In the large-backflow regime, the density modulation length becomes significantly reduced, rendering conventional fluorescence imaging increasingly challenging. In particular, states with very large backflow flux may require alternative density extraction protocols, which are beyond the scope of the present work. Nevertheless, our scheme demonstrates the capability to prepare such strongly backflowing states, paving the way for future experimental developments.

[1] Mikel Palmero, E Torrontegui, Juan Gonzalo Muga, and Michelle Modugno. Detecting quantum backflow by the density of a bose-einstein condensate. *Physical Review A—Atomic, Molecular, and Optical Physics*, 87(5):053618, 2013.

[2] Gordon R Allcock. The time of arrival in quantum mechanics ii. the individual measurement. *Annals of Physics*, 53(2):286–310, 1969.

[3] AJ Bracken and GF Melloy. Probability backflow and a new dimensionless quantum number. *Journal of Physics A: Mathematical and General*, 27(6):2197,

1994.

[4] Markus Penz, Gebhard Grübl, Sabine Kreidl, and Peter Wagner. A new approach to quantum backflow. *Journal of Physics A: Mathematical and General*, 39(2):423, 2005.

[5] MV Berry. Quantum backflow, negative kinetic energy, and optical retro-propagation. *Journal of Physics A: Mathematical and Theoretical*, 43(41):415302, 2010.

[6] Wytse van Dijk and F Masafumi Toyama. Decay of a quasistable quantum system and quantum backflow. *Physical Review A*, 100(5):052101, 2019.

[7] Paul Strange. Large quantum probability backflow and the azimuthal angle-angular momentum uncertainty relation for an electron in a constant magnetic field. *European journal of physics*, 33(5):1147, 2012.

[8] Arseni Goussev. Quantum backflow in a ring. *Physical Review A*, 103(2):022217, 2021.

[9] Arseni Goussev, Felix Quinque, Jaewoo Joo, and Andrew Burbanks. Quantum backflow current in a ring: Optimal bounds and fractality. *Physical Review A*, 110(2):022216, 2024.

[10] Maximilien Barbier, Arseni Goussev, and Shashi CL Srivastava. Unbounded quantum backflow in two dimensions. *Physical Review A*, 107(3):032204, 2023.

[11] Valentin Daniel Paccoia, Orlando Panella, and Pinaki Roy. Angular momentum quantum backflow in the noncommutative plane. *Physical Review A*, 102(6):062218, 2020.

[12] SV Mousavi and Salvador Miret-Artés. Dissipative quantum backflow. *The European Physical Journal Plus*, 135(3):1–18, 2020.

[13] SV Mousavi and Salvador Miret-Artés. Quantum backflow for dissipative two-identical-particle systems. *Results in Physics*, 19:103426, 2020.

[14] S. Mousavi and S. Miret-Artés. Erratum to: Dissipative quantum backflow. *The European Physical Journal Plus*, 135, 08 2020.

[15] Henning Bostelmann, Daniela Cadamuro, and Gandal夫 Lechner. Quantum backflow and scattering. *Physical Review A*, 96(1):012112, 2017.

[16] Alexandre Hefren de Vasconcelos Junior. *Quantum backflow in the presence of defects*. PhD thesis, University of York, 2021.

[17] Maximilien Barbier. Quantum backflow for many-particle systems. *arXiv preprint arXiv:2005.14685*, 2020.

[18] Maximilien Barbier and Arseni Goussev. Quantum backflow for two identical particles. *New Journal of Physics*, 27(3):033011, 2025.

[19] Arseni Goussev and Gregory V Morozov. Searching for bloch wave packets with almost definite momentum direction. *Physical Review A*, 112(3):032223, 2025.

[20] Sh Mardonov, M Palmero, M Modugno, E Ya Sherman, and JG Muga. Interference of spin-orbit-coupled bose-einstein condensates. *Europhysics Letters*, 106(6):60004, 2014.

[21] Maximilien Barbier and Arseni Goussev. On the experiment-friendly formulation of quantum backflow. *Quantum*, 5:536, 2021.

[22] Marek Miller, Woo Chee Yuan, Rainer Dumke, and Tomasz Paterek. Experiment-friendly formulation of quantum backflow. *Quantum*, 5:379, 2021.

[23] Yaniv Eliezer, Thomas Zacharias, and Alon Babbad. Observation of optical backflow. *Optica*, 7(1):72–76, 2020.

[24] Anat Daniel, Bohnishikha Ghosh, Bernard Gorzkowski, and Radek Lapkiewicz. Demonstrating backflow in classical two beams' interference. *New Journal of Physics*, 24(12):123011, 2022.

[25] Bohnishikha Ghosh, Anat Daniel, Bernard Gorzkowski, and Radek Lapkiewicz. Azimuthal backflow in light carrying orbital angular momentum. *Optica*, 10(9):1217–1222, 2023.

[26] Zhen-Fei Zhang, Peng-Fei Huang, Shan-Chuan Dong, Yan-Xin Rong, Jin-Shi Xu, Yong-Jian Gu, and Ya Xiao. Observation of single-photon azimuthal backflow with weak measurement. *Optics Letters*, 50(2):333–336, 2025.

[27] Savas Dimopoulos, Peter W Graham, Jason M Hogan, and Mark A Kasevich. General relativistic effects in atom interferometry. *Physical Review D—Particles, Fields, Gravitation, and Cosmology*, 78(4):042003, 2008.

[28] Jan Rudolph, Thomas Wilkason, Megan Nantel, Hunter Swan, Connor M Holland, Yijun Jiang, Benjamin E Garber, Samuel P Carman, and Jason M Hogan. Large momentum transfer clock atom interferometry on the 689 nm intercombination line of strontium. *Physical review letters*, 124(8):083604, 2020.

[29] Simon Stellmer, Florian Schreck, and Thomas C Killian. *Degenerate quantum gases of strontium*. World Scientific, 2013.